The Journal of Chemical Physics ARTICLE pubs.aip.org/aip/jcp

Suppression of cracking in drying colloidal suspensions with chain-like particles

Cite as: J. Chem. Phys. 160, 164901 (2024); doi: 10.1063/5.0203112
Submitted: 9 February 2024 • Accepted: 3 April 2024 •
Published Online: 24 April 2024

Zhaoxia Niu,[1] Yiping Zhao,[2] Qiuting Zhang,[1] Zhiyuan Zhao,[3] Dengteng Ge,[2] Jiajia Zhou,[4,5,a)] and Ye Xu[1,a)]

AFFILIATIONS

[1] School of Mechanical Engineering and Automation, Beihang University, Beijing 100191, China
[2] Institute for Engineering and Technology, Xinxing Cathay International Group, Shanghai 201403, China
[3] Wenzhou Institute, University of Chinese Academy of Science, Wenzhou, Zhejiang 325000, China
[4] South China Advanced Institute for Soft Matter Science and Technology, School of Emergent Soft Matter, South China University of Technology, Guangzhou 510640, China
[5] Guangdong Provincial Key Laboratory of Functional and Intelligent Hybrid Materials and Devices, South China University of Technology, Guangzhou 510640, China

[a)] **Authors to whom correspondence should be addressed:** zhouj2@scut.edu.cn and ye.xu@buaa.edu.cn

ABSTRACT

The prevention of drying-induced cracking is crucial in maintaining the mechanical integrity and functionality of colloidal deposits and coatings. Despite exploring various approaches, controlling drying-induced cracking remains a subject of great scientific interest and practical importance. By introducing chain-like particles composed of the same material and with comparable size into commonly used colloidal suspensions of spherical silica nanoparticles, we can significantly reduce the cracks formed in dried particle deposits and achieve a fivefold increase in the critical cracking thickness of colloidal silica coatings. The mechanism underlying the crack suppression is attributed to the increased porosity and pore sizes in dried particle deposits containing chain-like particle, which essentially leads to reduction in internal stresses developed during the drying process. Meanwhile, the nanoindentation measurements reveal that colloidal deposits with chain-like particles exhibit a smaller reduction in hardness compared to those reported using other cracking suppression approaches. This work demonstrates a promising technique for preparing colloidal coatings with enhanced crack resistance while maintaining desirable mechanical properties.

INTRODUCTION

The drying process of colloidal suspensions is an important step in the fabrication of coatings across various applications, including paintings,[1] photonic crystals,[2] batteries,[3] and other protective or functional coatings.[4] However, cracks commonly occur during drying, compromising the functionality, performance, and large-area fabrication of coatings, thus posing a substantial challenge in diverse technological domains.[5,6] Therefore, extensive research efforts have been directed toward understanding the underlying mechanisms of drying-induced cracking and developing corresponding methods to effectively reduce and eliminate these cracks.

As commonly understood, crack formation during the drying process results from the interplay between capillary pressure-induced shrinkage in colloidal deposits and constraints applied by the solid substrate. As a result, internal stresses inside the colloidal deposits build up and eventually lead to cracking when the stresses exceed a critical level. Correspondingly, strategies to avoid cracking in drying colloidal deposits have been developed based on the following three aspects: reducing capillary pressure, releasing the internal stress accumulated during drying process, and enhancing the fracture toughness of colloidal deposits. Reducing the capillary pressure can be achieved by decreasing the evaporation rate[7] and introducing the secondary immiscible liquid.[5] The internal stress accumulated during the drying process can be released by adjusting the substrate stiffness to loosen its constraints on drying-induced shrinkage[8] and introducing soft particles that can deform plastically.[9,10] The fracture toughness of the colloidal deposits can

be increased by adding polymer binders[11] and plasticizers.[12] While effective in certain applications, there are still technical issues that need to be overcome. For example, the addition of polymer binders[11] and soft particles[9,10] are common solutions in the paint industry. However, introducing polymer binders is greatly constrained by environmental concerns over the usage of the volatile organic content (VOC). Introducing soft particles can significantly reduce the elastic modulus and hardness of the colloidal deposits.[13]

Recently, introducing particles with various shapes and sizes to induce internal heterogeneity in colloidal coatings has been proposed as a new approach in reducing drying cracks.[14] Qiao *et al.*[15] show that introducing halloysite nanotubes in latex particle deposits can obtain a thicker crack-free colloidal deposit. Zhang *et al.*[16] demonstrate that the anisotropic particles can toughen the colloidal deposits by suppressing the formation of shear bands. Compared to the methods mentioned above, introducing anisotropic particles show potential advantages in reducing VOC addition and ensuring hardness of colloidal deposits. However, the crack pattern of the colloidal deposits with the anisotropic particles and the underlying mechanism in preventing cracks has still not been fully investigated.

Here, we investigate the cracking behaviors of colloidal suspensions with a mixture of spherical and chain-like silica nanoparticles. We prepare drops of colloidal suspension with different fractions of chain-like particles. The crack patterns formed in the dried particle deposits are observed and quantified. The porous structure of the dried colloidal deposits is characterized and key structure parameters, including porosity and pore size distribution, are extracted. Based on the experimental measurements, we utilize the fracture mechanics and the poroelastic theory to estimate the internal stresses developed during the drying process and propose the mechanism for the crack suppression due to the addition of chain-like particles. In addition, we also test the effect of adding chain-like particles in the cracking behaviors and mechanical properties of dried colloidal coatings. Our results provide new insights into how non-spherical particles affect the drying-induced cracking in colloidal deposits and demonstrate a new approach in crack suppression in drying colloidal coating applications.

RESULTS AND DISCUSSION

The suppression of cracks in dried colloidal deposits by the addition of chain-like particles

The colloidal suspensions employed in the current work are prepared by mixing spherical and chain-like silica particles in various fractions. The chain-like particles appear as strings composed of small sphere seed particles connected together. The morphology of those particles is shown in the micrographs obtained by using transmission electron microscopy (TEM), as shown in Fig. 1(a). The chain structures of those particles are also shown in the scanning electron microscopy (SEM) images in Fig. S1(a). The diameter of the chain-like particles is 10 ± 2 nm, as measured from the TEM micrographs. The length of the chain-like particles, measured by dynamic light scattering (DLS) using the Malvern Zetasizer Nano ZS90, is determined to be 117 ± 3 nm. For spherical particles, we use the commercially available silica particles, LUDOX HS-30. Those particles have an average diameter of 13 ± 3 nm, as measured from the TEM images [Fig. 1(a)], which is comparable to that of chain-like particles. More details regarding the colloidal particles and suspension are provided in Materials and Methods. Colloidal suspensions containing a mixture of chain-like and spherical particles are prepared by mixing two types of suspensions together at various volume ratios. For the following studies, we use five colloidal suspensions in which the weight percentage of the particles is kept as 16 wt. %, while the volume fractions of the chain-like particles in solid contents, ϕ_c, are 0, 0.3, 0.5, 0.7, and 1, respectively.

We investigated crack patterns in the particle deposits dried from suspensions containing different fractions of spherical and chain-like particles. For each colloidal suspension with different ϕ_c, 1 μl drops were deposited and dried on a cover glass, as shown in Fig. 1(a). The contact angles of the five colloidal suspension drops are similar (see Fig. S3), indicating consistent wetting properties. After evaporation of the colloidal suspension drops, distinct crack patterns appear in the dried colloidal deposits. In the colloidal deposits with only spherical particles, i.e., $\phi_c = 0$, typical radial cracks with regular spacing are observed, as shown in Fig. 1(b). As ϕ_c increases to 0.3, cracks exhibit similar radial patterns, but the number of cracks is reduced by ~50%. With further increase in ϕ_c, the number of radical cracks continues to reduce and the cracks become curved. For the deposits with chain-like particles only, i.e., $\phi_c = 1$, no radial cracks are observed, as shown in Fig. 1(f). Instead, only one circular crack is visible near the edge of the particle deposit, while the center region remains crack-free. To quantify the observed crack patterns in particle deposits with different ϕ_c, we count the number of radial cracks, N_c, and define the crack spacing, w, as the average distance between two radial cracks at the edge of the colloidal deposit, normalized by the perimeter l. Both N_c and w/l are plotted as a function of ϕ_c in Fig. 1(g). The results clearly indicate that the addition of chain-like particles significantly suppresses drying-induced cracks in colloidal suspension drops.

We also recorded the dynamic process of crack initiation and growth in the colloidal deposits with ϕ_c = 0, 0.5, and 1. Micrographs of drying and cracking drops at representative time points are shown in Fig. 2. As water evaporates, the colloidal particles consolidate and pack continuously toward the edge of the drop, while the three-phase contact line remains pinned at the edge. After a few minutes, the consolidation front, which is the boundary between the consolidated and dilute regions,[17,18] gradually appears and advances toward the center of the drop, as marked by the blue arrows shown in Fig. 2. For the case without chain-like particles, i.e., $\phi_c = 0$, the cracks originate from the edge of the drop and grow perpendicular to the consolidation front, as shown in Fig. 2(a). Eventually, a dried deposit with multiple radial cracks with regular spacing is formed. A similar cracking process is also seen for the drop with $\phi_c = 0.5$, as shown in Fig. 2(b), but with the final radial cracks in wide space and arc shapes. For the drop with $\phi_c = 1$, although still initiating at the edge, as shown in Fig. 2(c), a single crack grows along the periphery of the drop, forming a circle crack. No further crack is observed in the central region of the drop even though the consolidation front moves all the way across the drop. The observations clearly indicate that the introduction of chain-like particles in colloidal particle deposits crack initiation and growth in the drying colloidal suspension drop, leading to distinct crack patterns. The time-lapse videos showing the dynamic processes of consolidation and cracking in

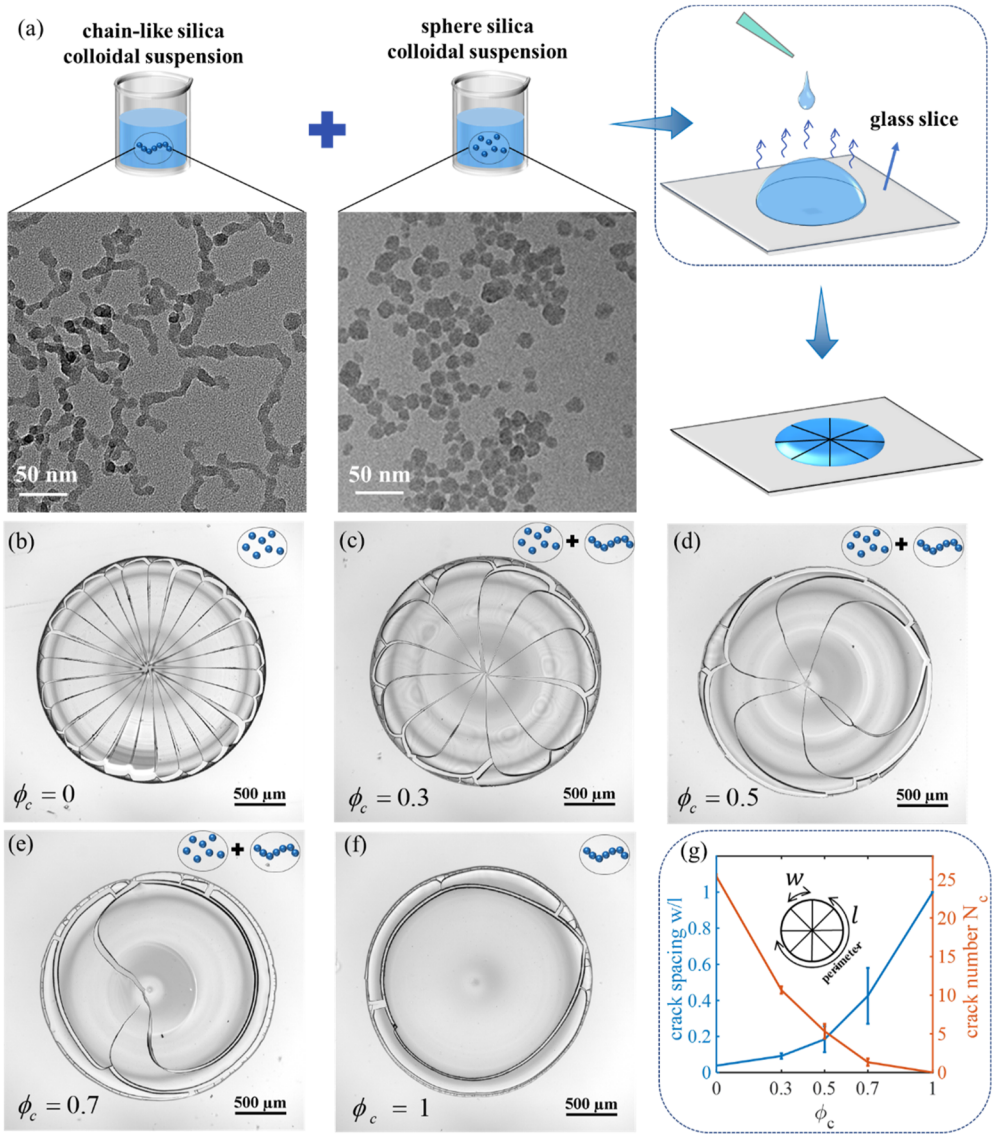

FIG. 1. Observation of the crack patterns in colloidal deposits with chain-like particles. (a) Schematic of the drying experiment setup of a colloidal drop. (b)–(f) Crack patterns in colloidal deposits with different ϕ_c (ϕ_c = 0, 0.3, 0.5, 0.7, and 1, respectively). (g) Crack spacing and crack numbers vs ϕ_c.

colloidal deposits with different ϕ_c are presented in Movies S1–S3 in the supplementary material. It is also worth noting that no obvious change in the total drying time is observed with the addition of chain-like particles.

Microstructure of colloidal deposits with chain-like particles

In order to better understand the effect of adding chain-like particles on the crack formation behaviors of colloidal deposits, we characterize the micro-structures of colloidal deposits with various ϕ_c. First, the microscopic morphologies of the packed structure in particle deposits with $\phi_c = 0$ and $\phi_c = 1$ are investigated by imaging the fracture surface of the colloidal suspension dried in 12-well plates using SEM (see Materials and Methods for more details). From the micrographs shown in Figs. 3(a) and 3(b), particles in the case of $\phi_c = 0$ are closely packed, whereas the particles in the case of $\phi_c = 1$ are packed in cross and intertwined patterns, resulting in a loose and porous structure. Such a difference aligns consistently with the structures observed on the surface of colloidal deposits dried on the glass substrates, as shown in Fig. S4. It is also worth noting that the SEM images of the colloidal deposits for $\phi_c = 0.5$ show no visible

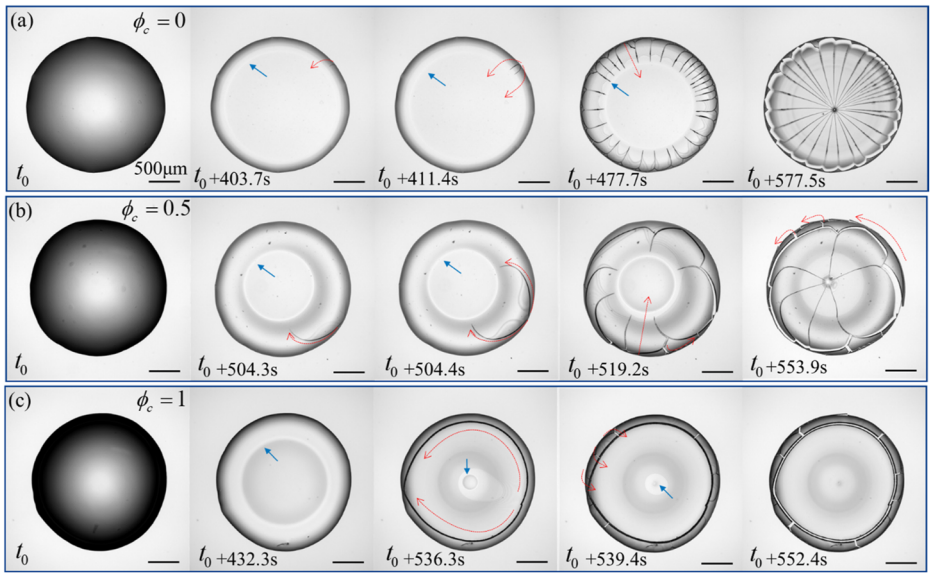

FIG. 2. Drying process of colloidal drops with chain-like particles. (a)–(c) Temporal evolution of crack patterns in colloidal deposits with ϕ_c = 0, 0.5, and 1, respectively. The initial time of the colloidal suspension drop depositing on the cover slice is marked as t_0. The blue arrows point to the consolidation front, and the red arrows point to the direction of the crack growth.

phase separation (see Fig. S8), indicating uniform blending of spherical and chain-like particles in the dried deposits of mixed colloidal suspensions.

To quantify the structure of the packed particles, we measure porosity, specific surface area, and pore diameter distribution

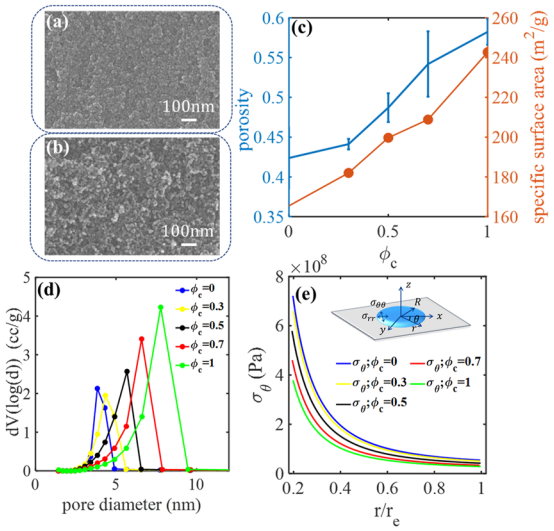

FIG. 3. Microstructure and stress development of colloidal deposits with chain-like particles. (a) and (b) SEM images in colloidal deposits with ϕ_c = 0 and ϕ_c = 1, respectively. (c) Porosity and specific surface area of dried particle deposits as a function of ϕ_c. (d) Distribution of pore size distribution in colloidal deposits with various ϕ_c. (d) Distribution of the hoop stress, σ_θ in colloidal deposits with various ϕ_c.

of the colloidal deposits with different ϕ_c. The porosity, ψ_p, is evaluated by

$$\psi_p = 1 - \frac{V_p}{V_d} = 1 - \frac{m_p/m_d}{V_d}, \tag{1}$$

where V_p and V_d represent the volumes of colloidal particles and dried colloidal deposits, respectively. Here, V_p is calculated using the mass (m_p) and density of the colloidal silica particles (ρ_p = 2.6 g/cm^3), while V_d is evaluated from the thickness and area of the colloidal deposits captured by camera (see Sec. IV). We find the calculated porosity of the colloidal deposit increases with ϕ_c, as shown in Fig. 3(c). In details, when ϕ_c = 0, the porosity is 0.42 ± 0.04 and the corresponding packing fraction of the colloidal particles is $\psi_d = 1 - \psi_p = 0.58 \pm 0.04$. Such a value indicates that the colloidal particles are nearly closely packed.[19] With the addition of chain-like particles, when ϕ_c = 1, ψ_p increases and reaches 0.58 ± 0.02, indicating a more loosely packed structure of the colloidal deposits containing chain-like particles. The result of porosity is in accordance with the SEM images shown in Figs. 3(a) and 3(b). In addition, the specific surface area and the pore diameter distribution are measured by nitrogen adsorption. The nitrogen adsorption–desorption isotherms, as shown in Fig. S9(a), exhibit a type IV isotherm as defined by IUPAC,[20,21] which is commonly observed in mesoporous silica materials.[22] The H2 type hysteresis loops reveal cage-type mesopores within all colloidal deposits.[23] The specific surface areas are then calculated using the multi-point Brunauer–Emmett–Teller (BET) model, and the results are shown in Fig. 3(b). Similar to the trend of porosity, the specific surface area monotonically increases with ϕ_c, suggesting the existence of

more pores in the colloidal deposits with higher fractions of chain-like particles. Moreover, we obtained the pore size distributions for various ϕ_c using the Barrett–Joyner–Halenda (BJH) approach from the adsorption–desorption isotherms,[23] as shown in Fig. 3(c). The measured pore sizes for all particle deposits span from 2 to 10 nm, falling within the mesoporous range. The peak area of the distributions correlates with the diversity of the pore size.[24] It is evident that the peak area expands with increasing ϕ_c, indicating that the addition of chain-like particles in colloidal deposits leads to improved diversity of pore diameters. The peak value of the pore size distribution in Fig. 3(c) (i.e., the most probable pore size) increases with the rising value of ϕ_c, as extracted and shown in Fig. S9(b). Therefore, the addition of chain-like particles results in distinct microstructure characteristics of colloidal deposits, which may affect the accumulation of drying-induced stress.

With the information of particle packing structure modified with the addition of chain-like particles, we utilize a poroelastic model to interpret the change of the crack pattern in colloidal deposits with various ϕ_c. Due to their circular, flat, and thin porous structure, the colloidal deposits can be modeled in a cylindrical coordinate (r, θ, z). During the drying process of the colloidal suspension drop, the liquid pressure from the porous colloidal deposits compacts the deposits behind the consolidation front. Consequently, the stresses accumulate as the liquid pressure evolves over time. Inside the deposit, the volume of water is conserved. The permeability is almost constant due to the uniform packing fraction of colloidal deposits. The liquid pressure satisfies the Laplace equation,[17,18]

$$\nabla^2 P_L(r) = 0. \tag{2}$$

To obtain the liquid pressure, two boundary conditions are required. The liquid pressure at the drop edge has a maximum of capillary pressure $P_{\max}$. Beyond this, the liquid menisci recede into the porous deposits, limiting the deformation of the deposits.[25] In principle, cracks are formed from the edge of the colloidal deposits, as shown in Fig. 2. Therefore, we can assume that cracks in the colloidal deposits can form as soon as the liquid pressure in the boundary of drop is close to $P_{\max}$ ($r = r_e$, where r_e is drop radius pinned at the contact line.),[26] that is,

$$P_L(r)|_{r=r_e} = -P_{\max}. \tag{3}$$

Here, $P_{\max}$ depends on the wetting characteristics of the solvent by $(-P_{\max})a/2\gamma = 3\cos\theta\psi_d/2(1-\psi_d)$, where θ is the wetting angle and approximates 35° for the wetting angle between the silica particles and water.[27] According to Darcy's law, the gradient of liquid pressure develops in the form of

$$\frac{\partial P_L(r)}{\partial r}|_{r=r_e} = -\frac{J_s\eta}{k}, \tag{4}$$

where J_s is the evaporation rate. The permeability of the colloidal deposits k is given[7] by $k = \frac{2a^2(1-\psi_d)}{75\psi_d^2}$. Both of these boundary conditions depend on the packing fraction ψ_d ($\psi_d = 1 - \psi_p$). Solving the Laplace Eq. (2) with boundary conditions (3) and (4), we obtain the liquid pressure,

$$P_L(r) = -\frac{J_s\eta r_e}{k}\ln\left(\frac{r}{r_e}\right) - P_{\max}. \tag{5}$$

Here, the liquid pressure and the packing fraction ψ_d are correlated through the permeability k and the Laplace pressure $P_{\max}$. Knowing the water pressure, we can then calculate the stress distribution inside the deposit. The equilibrium stresses σ_r (radial stress) and σ_θ (hoop stress) in the cylindrical coordinate system (r, θ, z), resulting in crack formation of colloidal deposit in a gel-like state can be given from the following equation:[28]

$$\sigma_\theta = \sigma_r + r\frac{\partial\sigma_r}{\partial r}. \tag{6}$$

The stress, strain, and the liquid pressure are correlated by Biot's constitutive relation.[29] Based on the constitutive relation, previous studies[30,31] have calculated the stress distributions of the ring colloidal deposits and dense bacterial drop deposits. The colloidal deposit in our work has a similar geometry. Therefore, we invoke the similar assumptions and the constitutive relation in our work. Under the assumptions of axial stress $\sigma_z = 0$ and $\epsilon_z \gg \epsilon_r + \epsilon_\theta$, with the boundary conditions of $\sigma_r|_{r=r_e} \approx 0$ and Biot's constitutive relation, the hoop stress on stiffness substrate can be given by[30,31]

$$\sigma_\theta = B\left(\frac{1}{2}\ln\frac{r}{r_e} + \frac{1}{4} - \frac{r_e^2}{4r^2}\right) + \frac{A(-P_{\max})}{2}\left(1 + \frac{r_e^2}{r^2}\right), \tag{7}$$

where $A = -\frac{2}{3K(\frac{1}{3K}+\frac{\nu}{E})}$ and $B = -\frac{Ar_eJ_s\eta}{k}$. K is bulk modulus of the deposits, and ν is Poisson's ratio.[1] The detailed derivation is given in the supplementary material. The hoop stress shown in Fig. 3(e) $\sigma_z > 0$ is tensile, resulting in radial cracks in the colloidal deposits. However, the reduction in ψ_d, or equivalently, the rise in porosity resulting from the increasing ϕ_c in colloidal deposits, leads to a decrease in hoop stress. The decrease in hoop stress aligns with the transition of crack pattern in colloidal deposits that w/l increases and N_c decreases. Therefore, the ϕ_c-dependent transition of crack patterns in dried colloidal deposits is attributed to the reduction in hoop stress, resulting from the increase in porosity.

Critical cracking thickness and mechanical properties of colloidal deposits with chain-like particles

In addition to the observations of crack patterns in dried drops of colloidal suspension, we also investigate the crack suppression effect of the chain-like particles in colloidal coatings. In the colloidal coating applications, the critical cracking thickness (CCT) is usually used to evaluate the resistance of drying-induced cracking.[32,33] Therefore, we quantified the CCT in colloidal coatings containing different fractions of chain-like particles. Specifically, for each colloidal suspension of different ϕ_c, we use spin-coating to prepare coatings with a series of thicknesses and observe their cracking behaviors upon drying. The relationship between the spin-coating speed and the final coating thickness are shown in Fig. S10(a). Representative crack patterns of colloidal coatings with $\phi_c = 0$, 0.5, and 1 at various thicknesses are shown in Fig. 4(a). While colloidal coatings can remain crack-free at smaller thicknesses, cracks start to appear

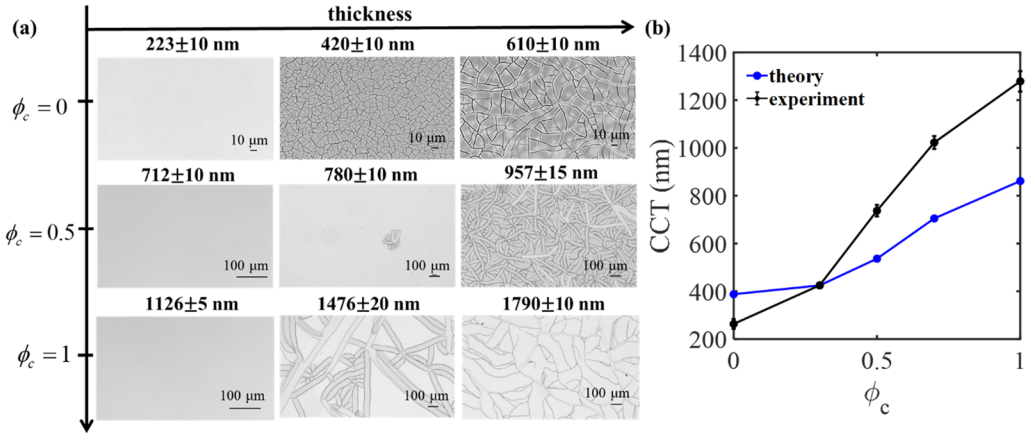

FIG. 4. Critical cracking thickness of colloidal deposits with various ϕ_c. (a) Optical microscopic images of colloidal deposits with ϕ_c = 0, 0.5, and 1, respectively. (b) Critical cracking thickness from experimental characterization and theoretical analyses of colloidal deposits with various ϕ_c.

when the thickness increases. However, the colloidal coatings with the addition of chain-like particles are able to remain crack-free at a higher thickness than that of only spherical silica particles. It is also interesting to observe that the crack pattern transitions from polygons in colloidal coatings with $\phi_c = 0$ into intertwined strips in those mixed with chain-like particles. This unique crack pattern has been reported in baked coatings of trimethylsiloxane and is the result of the collaborative behaviors of delamination and crack propagation.[34] For each ϕ_c, the CCT is determined as the thickness of the thinnest coating without visible cracks. As shown in Fig. 4(b), the CCT increases with ϕ_c, clearly indicating that the addition of chain-like particles can significantly reduce cracking in drying colloidal coatings.

The critical cracking thickness in drying colloidal coatings can be theoretically analyzed and predicted based on a continuum approach. The cracking of colloidal deposits can be interpreted as the result of a mismatch between the elastic modulus of the porous elastic film and the rigid substrate. According to Griffith's criterion for equilibrium crack propagation along with the nonlinear stress–strain relation[35] for a colloidal deposit of identical elastic spheres, Tirumkudulu and Russel derived the critical stress for the nucleation of an isolated crack,[36]

$$\frac{\sigma_c a}{2\gamma} = 0.1877\left(\frac{2a}{h_c}\right)^{2/3}\left(\frac{GM\psi_d a}{2\gamma}\right)^{1/3}. \tag{8}$$

Here, a represents the particle radius, γ is the surface tension, h_c is the critical cracking thickness, G is the shear modulus of the particles (G = 31 GPa for silica particles[25]), and M is the coordination number (M = 5; details are shown in the supplementary material).[37] The biaxial stress and the pressure in the pores P_L can be correlated by Biot's constitutive relation,[32,38] $\sigma = -\frac{3}{4} \times P_L$. The critical stress σ_c is reached when the water pressure P_L reaches the corresponding maximum capillary pressure $P_{\max}$, which is given by $([-P_{\max}]a/2\gamma = 3\cos\theta\psi_d/2[1-\psi_d])$ according to the calculation performed by Singh and Tirumkudulu.[25] Therefore, the critical cracking thickness h_c is given by

$$h_c = \xi \times \left[\frac{GM\psi_d a^3}{2\gamma}\right]^{1/2}\left[\frac{2\gamma}{-P_{\max}a}\right]^{3/2}. \tag{9}$$

Here, ξ is a constant. In prior studies,[25] ξ equals to 0.64 resulted in improved alignment between the theory and experiments. Here, in line with our own experimental findings, we have observed that setting ξ = 2 yields a better fit. The detailed information can be referred to in the supplementary material.

The CCT for the colloidal deposits with different ϕ_c can be predicted by substituting ψ_d, $\gamma \sim 0.07$, $G \sim 31$ GPa, $a \sim 6.5$ nm, and $M \sim 5$ into Eq. (9). The results are shown in Fig. 4(b). The predicted CCT exhibits an upward trend with the rising ϕ_c, as shown in Fig. 4(b), which is in accordance with the experimentally measured result. The theoretical model suggests a linear relationship between the CCT and $\sqrt{(1-\psi_d)^3/\psi_d^2}$. As ψ_d decreases, there is a corresponding reduction in the CCT. In our experiment, increasing ϕ_c in the colloidal deposits leads to a reduction in ψ_d. Consequently, the CCT of colloidal deposits with different ϕ_c exhibits an ascent. Nevertheless, some discrepancies emerge between the theoretically predicted CCT and the experimental measured values. This discrepancy may be attributed to several experimental uncertainties, including the coordination number, pore diameter, and the packing structure of the chain-like particles, as discussed in the supplementary material. In addition, the model that we employed does not account for the effects of the shape of the chain-like particles and the resulting intertwined packing of these particles, which would likely hinder the crack propagation in particle deposits. These additional factors related to particle shape and packing structure could contribute to the underestimation of the CCT values by our model.

Finally, the mechanical properties of colloidal coatings are also characterized using the nano-indentation method. As shown in Fig. 5(a), both elastic modulus, E, and hardness, H, decrease when ϕ_c increases. The reduced elastic modulus from 15 to 3 GPa is likely attributed to the increase in porosity of colloidal deposits with the addition of chain-like particles, as the elastic modulus of the particle deposits is thought to be proportional to the packing fraction as

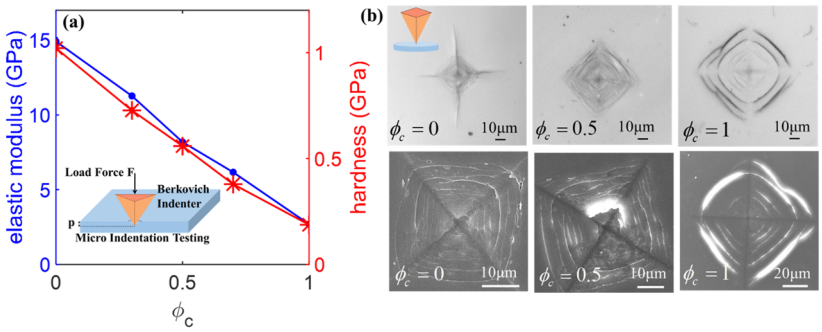

FIG. 5. Mechanical properties of colloidal deposits with ϕ_c. (a) Elastic modulus and hardness of colloidal deposits with various ϕ_c. (b) Optical and SEM micrographs of the residual indentation areas in colloidal deposits with various ϕ_c under the same loading.

$E \sim GM\psi_d$.[36] This linear relation between E and ψ_d is also confirmed by our experimental data shown in Fig. S11(b). Similarly, the hardness decreases from ~1–0.2 GPa, a factor of 5 reduction. In addition, the fracture toughness of the colloidal coatings is also qualitatively compared by imaging the residual indentation under the same loading. As shown in Fig. 5(b), radial cracks appear along the corners of the indentation in colloidal coatings with $\phi_c = 0$. For coatings with $\phi_c = 0.5$ and 1, while the residual indentation area increases with an increase in ϕ_c, which is in agreement with the reduction in the hardness, no radical crack is observed. This result suggests that the fracture toughness of the colloidal coating increases with the addition of chain-like particles. This is another evidence for the crack suppression effect of adding chain-like particles.

We would like to point out that the addition of different colloidals for drying crack reduction has been explored in previous studies. For example, adding soft styrene–acrylic particles (particles with glass transition temperature below the room temperature, $T = 6\,^{\circ}\mathrm{C}$) in colloidal suspension of silica indeed suppresses cracking in dried colloidal coatings.[13] However, it results in a drastic reduction in hardness (by at least one order of magnitude) of the coatings. The addition of halloysite nanotubes in polymer latex can also increase the critical cracking thickness of the coating;[15] however, it leads to a significant increase in the drying time. In comparison, in this work, our colloidal coatings mixed with chain-like particles exhibit a much smaller reduction (factor of 3–5) in the elastic modulus and hardness when similar cracking suppression effects are achieved. Meanwhile, the drying time of colloidal suspension with chain-like particles exhibits minimal variation. Therefore, the addition of chain-like particles made of the same material, hence with the same mechanical properties, into colloidal suspensions serves as a promising method in suppressing crack formation while maintaining desirable mechanical properties of the colloidal coating.

CONCLUSIONS

In summary, we demonstrate a new method of crack suppression in colloidal coatings by introducing chain-like particles into the colloidal suspension of spherical particles. We confirmed that the addition of chain-like particles can significantly suppress the formation of drying-induced cracks, both colloidal suspension drops and colloidal coatings. The characterization of pore structures reveals that the addition of those chain-like particles results in particle deposits with high porosity and larger pore sizes. We hypothesis that this change of microstructure leads to the decrease in drying-induced capillary pressure acting on the particle deposits, therefore, reducing the internal tensile stresses developed during the drying process. As a result, the critical cracking thickness of the colloidal coatings can be increased with the addition of chain-like particles. More importantly, the cracking suppression in this work is achieved at a smaller cost of hardness reduction in the colloidal coating and increase in drying time, as compared to other methods. Therefore, our work demonstrates a promising method in preparing crack-resistant colloidal coatings with balanced mechanical properties and a processing window.

MATERIALS AND METHODS

Colloidal suspension

Aqueous suspensions of monodisperse sphere colloidal silica nanoparticles (LUDOX HS-30) were purchased from Sigma-Aldrich. The initial concentration is 30 wt. % (~14 vol. %), which is then diluted to 16 wt. % (~7 vol. %) by deionized water. The morphologies and particle size distributions are obtained from SEM images and TEM images, as shown in Fig. S2. The chain-like silica colloidal particles were synthesized via the aggregation of sphere seed particles in the presence of amino acids.[39,40] The morphologies and particle diameter distributions are shown in Fig. S1. The chain-like silica particles were dispersed in deionized water. The initial concentration of all suspensions is set at 16 wt. %(~7 vol. %). The synthesis procedure is given in the supplementary material. Before the drying experiment, the prepared dispersion was kept in an ultrasonic bath for 6 min to ensure thorough mixing. All the drying experiments were performed under the glove box or ambient conditions at temperature $23 \pm 2\,^{\circ}\mathrm{C}$ and relative humidity $55\% \pm 4\%$.

Microscope observation

For the crack observation of the drop, a 1 μl colloidal suspension drop was deposited on a clean cover glass. The cover glasses were cleaned ultrasonically with soap solution and ethanol

for 30 min, respectively. The crack pattern and drying process were captured by an upright microscope (Eclipse Ci, Nikon) using a 4× objective lens (NA = 0.13). The drying process was recorded at about 62 ms intervals.

Characterization of pore structures

To obtain a thicker and more uniform testing specimen for the characterization of microstructures and mechanical properties, we dried the colloidal suspension in a well of 12-well plate with a diameter of 2.2 cm, as shown in the Fig. S5. The wetting properties of the colloidal suspensions and the crack patterns of dried colloidal deposits with chain-like particles are given in the supplementary material. The colloidal suspensions with five ϕ_c (ϕ_c = 0, 0.3, 0.5, 0.7, and 1) are dried at the same initial concentration (16 wt. %) and the same initial volume (1.5 ml).

To determine the porosity, we utilized a Canon 5D Mark 2 camera to capture both the area of the deposits and thickness of the fractured surface, using which the total volume of the deposit was calculated. The weight of the coatings was measured by using an electronic scale (JJ124BC 0.1 mg). Pore structure analysis was conducted through nitrogen adsorption–desorption experiments (Quantachrome Instruments).

Characterization of the critical cracking thickness (CCT)

In order to determine the critical cracking thickness (CCT), the silica colloidal suspensions were deposited onto the glass slide substrates by spin coating (MYCRO, WS650MZ) to form the uniform coatings. The glass slide substrates, cleaned using the previously mentioned procedure, were cut into squares (about 2.54 × 2.54 cm^2, $1'' \times 1''$) in advance. For better wetting, the glass substrates need to be cleaned by plasma (Harrick Plasma, PDC-32G-2) for 2 min. Then, ~600 μl of the colloidal suspension was deposited onto the glass substrates. Spinning coating was carried at a steady-state rotational speed for 1 min with an acceleration rate of 700 rpm/s. Colloidal coatings with various thicknesses were prepared by varying the rotational speed and the initial concentration of the colloidal suspension. The initial concentration of the colloidal deposits with ϕ_c = 0 are 10 and 16 wt. %, respectively, as shown in Fig. S10(b). The initial concentration of the colloidal deposits with other ϕ_c is consistent at 16 wt. %. The thickness of the deposits was measured using a surface profiler (KLA, Alpha-Step D600) at a load force of 2 μN, after removing a portion of the coatings from the substrate.

Indentation testing

The measurements of the mechanical properties were performed using a nanoindentation testing instrument (NHT3, Anton Paar) with a Berkovich indenter. The indenter was driven into the specimens with a loading speed of 20 mN min^{-1} until reaching a maximum load F = 10 mN. The curve of the load force and the penetration depth for colloidal deposits with different ϕ_c are shown in Fig. S11(a). The elastic modulus E and hardness are calculated from the initial slope of tangents of the unloading curve, according to the Oliver–Pharr method. The specimens were also indented by using the Vickers hardness tester (Falcon 500, Innovatest) with a Vickers indenter at a load force of 1 N. The indentation images were observed using an upright microscope with a 20× objective lens (NA = 0.5) in reflection mode. The high magnification images were also obtained using the SEM.

SUPPLEMENTARY MATERIAL

See the supplementary material for detailed description about the synthesis and characterization of colloidal particles, additional information on the setup of drying experiments and characterization of crack patterns, microstructure of colloidal deposits with chain-like particles and supplementary analysis on critical cracking thickness, and mechanical properties of colloidal deposits with chain-like particles.

Movie S1–S3: time-lapse video of crack patterns in colloidal deposits with ϕ_c = 0, 0.5, and 1, respectively. The movies are accelerated by 50 times.

ACKNOWLEDGMENTS

This work was supported by the National Natural Science Foundation of China (Grant Nos. NSFC 11674019, 12072010, and 22373036) and the Fundamental Research Funds for the Central Universities (Grant No. YWF-22-K-101).

AUTHOR DECLARATIONS

Conflict of Interest

The authors have no conflicts to disclose.

Author Contributions

Zhaoxia Niu: Conceptualization (equal); Data curation (equal); Formal analysis (equal); Investigation (equal); Methodology (equal); Project administration (equal); Validation (equal); Visualization (equal); Writing – original draft (equal); Writing – review & editing (equal). **Yiping Zhao**: Conceptualization (equal); Data curation (equal); Formal analysis (equal); Investigation (equal); Methodology (equal); Project administration (equal); Resources (equal); Validation (equal); Visualization (equal); Writing – original draft (equal); Writing – review & editing (equal). **Qiuting Zhang**: Investigation (equal); Methodology (equal); Resources (equal); Supervision (equal); Writing – review & editing (equal). **Zhiyuan Zhao**: Supervision (equal); Writing – review & editing (equal). **Dengteng Ge**: Methodology (equal); Resources (equal); Supervision (equal); Writing – review & editing (equal). **Jiajia Zhou**: Data curation (equal); Formal analysis (equal); Methodology (equal); Resources (equal); Supervision (equal); Writing – review & editing (equal). **Ye Xu**: Conceptualization (equal); Data curation (equal); Formal analysis (equal); Funding acquisition (lead); Methodology (equal); Project administration (lead); Supervision (lead); Writing – review & editing (equal).

DATA AVAILABILITY

The data that support the findings of this study are available from the corresponding authors upon reasonable request.

REFERENCES

[1] M. Léang, F. Giorgiutti-Dauphiné, L.-T. Lee, and L. Pauchard, "Crack opening: From colloidal systems to paintings," Soft Matter **13**(34), 5802–5808 (2017).
[2] B. Hatton, L. Mishchenko, S. Davis, K. H. Sandhage, and J. Aizenberg, "Assembly of large-area, highly ordered, crack-free inverse opal films," Proc. Natl. Acad. Sci. U. S. A. **107**(23), 10354–10359 (2010).
[3] L. Hu, H. Wu, F. La Mantia, Y. Yang, and Y. Cui, "Thin, flexible secondary Li-ion paper batteries," ACS Nano **4**(10), 5843–5848 (2010).
[4] Y. A. Vlasov, X.-Z. Bo, J. C. Sturm, and D. J. Norris, "On-chip natural assembly of silicon photonic bandgap crystals," Nature **414**(6861), 289–293 (2001).
[5] S. B. Fischer and E. Koos, "Using an added liquid to suppress drying defects in hard particle coatings," J. Colloid Interface Sci. **582**, 1231–1242 (2021).
[6] Q. Fu, B. Zhu, and J. Ge, "Hierarchically structured photonic crystals for integrated chemical separation and colorimetric detection," Nanoscale **9**(7), 2457–2463 (2017).
[7] W. P. Lee and A. F. Routh, "Why do drying films crack?," Langmuir **20**(23), 9885–9888 (2004).
[8] M. I. Smith and J. S. Sharp, "Effects of substrate constraint on crack pattern formation in thin films of colloidal polystyrene particles," Langmuir **27**(13), 8009–8017 (2011).
[9] F. Boulogne, F. Giorgiutti-Dauphiné, and L. Pauchard, "How to reduce the crack density in drying colloidal material?," Oil Gas Sci. Technol.–Rev. IFP Energies Nouvelles **69**(3), 397–404 (2014).
[10] D. Colombini, H. Hassander, O. J. Karlsson, and F. H. J. Maurer, "Influence of the particle size and particle size ratio on the morphology and viscoelastic properties of bimodal hard/soft latex blends," Macromolecules **37**(18), 6865–6873 (2004).
[11] M. Yamamura, "Adsorption-mediated nonlinearity of critical cracking thickness in drying nanoparticle–polymer suspensions," AIChE J. **67**(5), e17229 (2021).
[12] J. A. Lewis, "Colloidal processing of ceramics," J. Am. Ceram. Soc. **83**(10), 2341–2359 (2000).
[13] L. Yang, S. Zhou, G. Gu, and L. Wu, "Film-forming behavior and mechanical properties of colloidal silica/polymer latex blends with high silica load," J. Appl. Polym. Sci. **129**(3), 1434–1445 (2013).
[14] V. R. Dugyala and M. G. Basavaraj, "Self-assembly of nano-ellipsoids into ordered structures via vertical deposition," RSC Adv. **5**(74), 60079–60084 (2015).
[15] J. Qiao, J. Adams, and D. Johannsmann, "Addition of halloysite nanotubes prevents cracking in drying latex films," Langmuir **28**(23), 8674–8680 (2012).
[16] L. Zhang, G. Feng, Z. Zeravcic, T. Brugarolas, A. J. Liu, and D. Lee, "Using shape anisotropy to toughen disordered nanoparticle assemblies," ACS Nano **7**(9), 8043–8050 (2013).
[17] Z. Niu, H. Gao, M. Doi, J. Zhou, and Y. Xu, "Interplay of consolidation fronts and cracks in drying colloidal coatings and its application in controlling crack pattern formation," Langmuir **38**(45), 13880–13887 (2022).
[18] P. Lilin and I. Bischofberger, "Criteria for crack formation and air invasion in drying colloidal suspensions," Langmuir **38**, 7442 (2022).
[19] E. R. Dufresne, E. I. Corwin, N. A. Greenblatt, J. Ashmore, D. Y. Wang, A. D. Dinsmore, J. X. Cheng, X. S. Xie, J. W. Hutchinson, and D. A. Weitz, "Flow and fracture in drying nanoparticle suspensions," Phys. Rev. Lett. **91**(22), 224501 (2003).
[20] M. Thommes, K. Kaneko, A. V. Neimark, J. P. Olivier, F. Rodriguez-Reinoso, J. Rouquerol, and K. S. W. Sing, "Physisorption of gases, with special reference to the evaluation of surface area and pore size distribution (IUPAC technical report)," Pure Appl. Chem. **87**(9–10), 1051–1069 (2015).
[21] X. Wang, Y. Zhang, W. Luo, A. A. Elzatahry, X. Cheng, A. Alghamdi, A. M. Abdullah, Y. Deng, and D. Zhao, "Synthesis of ordered mesoporous silica with tunable morphologies and pore sizes via a nonpolar solvent-assisted Stöber method," Chem. Mater. **28**(7), 2356–2362 (2016).
[22] M. Jaroniec and L. A. Solovyov, "Improvement of the Kruk–Jaroniec–Sayari method for pore size analysis of ordered silicas with cylindrical mesopores," Langmuir **22**(16), 6757–6760 (2006).
[23] M. Kruk, M. Jaroniec, and A. Sayari, "Application of large pore MCM-41 molecular sieves to improve pore size analysis using nitrogen adsorption measurements," Langmuir **13**(23), 6267–6273 (1997).
[24] G. Ni, S. Li, S. Rahman, M. Xun, H. Wang, Y. Xu, and H. Xie, "Effect of nitric acid on the pore structure and fractal characteristics of coal based on the low-temperature nitrogen adsorption method," Powder Technol. **367**, 506–516 (2020).
[25] K. B. Singh and M. S. Tirumkudulu, "Cracking in drying colloidal films," Phys. Rev. Lett. **98**(21), 218302 (2007).
[26] H. Pingulkar and J.-B. Salmon, "Confined directional drying of a colloidal dispersion: Kinetic modeling," Soft Matter **19**, 2176 (2023).
[27] T. H. Muster, C. A. Prestidge, and R. A. Hayes, "Water adsorption kinetics and contact angles of silica particles," Colloids Surf., A **176**(2-3), 253–266 (2001).
[28] C. Allain and L. Limat, "Regular patterns of cracks formed by directional drying of a collodial suspension," Phys. Rev. Lett. **74**(15), 2981–2984 (1995).
[29] M. A. Biot, "General theory of three-dimensional consolidation," J. Appl. Phys. **12**(2), 155–164 (1941).
[30] H. Lama, T. Gogoi, M. G. Basavaraj, L. Pauchard, and D. K. Satapathy, "Synergy between the crack pattern and substrate elasticity in colloidal deposits," Phys. Rev. E **103**(3), 032602 (2021).
[31] X. Ma, Z. Liu, W. Zeng, T. Lin, X. Tian, and X. Cheng, "Crack patterns of drying dense bacterial suspensions," Soft Matter **18**(28), 5239–5248 (2022).
[32] B. S. Tomar and M. S. Tirumkudulu, "Critical cracking thickness of drying polymer films," Soft Matter **19**(21), 3910–3916 (2023).
[33] J. H. Prosser, T. Brugarolas, S. Lee, A. J. Nolte, and D. Lee, "Avoiding cracks in nanoparticle films," Nano Lett. **12**(10), 5287–5291 (2012).
[34] J. Marthelot, B. Roman, J. Bico, J. Teisseire, D. Dalmas, and F. Melo, "Self-replicating cracks: A collaborative fracture mode in thin films," Phys. Rev. Lett. **113**(8), 085502 (2014).
[35] A. F. Routh and W. B. Russel, "A process model for latex film formation: Limiting regimes for individual driving forces," Langmuir **15**(22), 7762–7773 (1999).
[36] M. S. Tirumkudulu and W. B. Russel, "Cracking in drying latex films," Langmuir **21**(11), 4938–4948 (2005).
[37] K. Yasuda, F. Takase, and Y. Matsuo, "Stochastic analysis on coordination number distribution of particles during powder compaction," Adv. Powder Technol. **24**(5), 871–878 (2013).
[38] M. A. Biot, "Theory of elasticity and consolidation for a porous anisotropic solid," J. Appl. Phys. **26**(2), 182–185 (1955).
[39] J. Wang, A. Sugawara, A. Shimojima, and T. Okubo, "Preparation of anisotropic silica nanoparticles via controlled assembly of presynthesized spherical seeds," Langmuir **26**(23), 18491–18498 (2010).
[40] Y. Zhao, Z. Wang, Y. Lv, S. Li, W. Ge, C. He, L. Yang, and D. Ge, "Conformal fabrication of thick superhydrophobic coatings via reduction of sorption barrier against multiple damages," Surf. Coat. Technol. **444**, 128658 (2022).

Supporting Information：

Suppression of cracking in drying colloidal suspensions with chain-like particles

Zhaoxia Niu,[1] Yiping Zhao[2], Qiuting Zhang,[1] Zhiyuan Zhao,[3] Dengteng Ge[2], Jiajia Zhou,[4,5] Ye Xu[1,*]

[1]*School of Mechanical Engineering and Automation, Beihang University, Beijing 100191, China;*

[2]*Institute for Engineering and Technology , Xinxing Cathay International Group, Shanghai 201403,China;*

[3]*Wenzhou Institute, University of Chinese Academy of Science, Wenzhou, Zhejiang 325000, China;*

[4] *South China Advanced Institute for Soft Matter Science and Technology, School of Emergent Soft Matter, South China University of Technology, Guangzhou 510640, China;*

[5]*Guangdong Provincial Key Laboratory of Functional and Intelligent Hybrid Materials and Devices, South China University of Technology, Guangzhou 510640, China*

*Email: zhouj2@scut.edu.cn, ye.xu@buaa.edu.cn

1. Supplementary Movies

MovieS1: Time-lapse video of crack patterns in colloidal deposits with $\phi_c = 0$. The movie is accelerated by 50 times.

MovieS2: Time-lapse video of crack patterns in colloidal deposits with $\phi_c = 0.5$. The movie is accelerated by 50 times.

MovieS3: Time-lapse video of crack patterns in colloidal deposits with $\phi_c = 1$. The movie is accelerated by 50 times.

2. Supplementary Figures

Synthesis and characterization of colloidal particles

The chain-like particles were synthesized by a two-step process. Firstly, to prepare the silica particle seed suspension, we added 54.6 mg L-arginine (Sinopharm Chemical Reagent Co., Ltd.) and 3.13 g TEOS (tetraethylorthosilicate, Sinopharm Chemical Reagent Co., Ltd.) into 41.4 g deionized water and kept stirring at 60 ℃ for 24 h. Then, for the preparation of chain-like silica particles, we added 0.213 g L-arginine, 8 g silica particle seed suspension, 10 g deionized water, and 0.78 g TEOS into 65 g ethanol (Sinopharm Chemical Reagent Co., Ltd) and kept stirring at 60 ℃ for 12 h. After that, the chain-like particles were dispersed in deionized water at a concentration of 16 wt. %. The characterizations of chain-like silica particles are shown in Figures S1, in terms of the Scanning Electron Microscopy (SEM) and Transmission Electron Microscopy (TEM) micrographs.

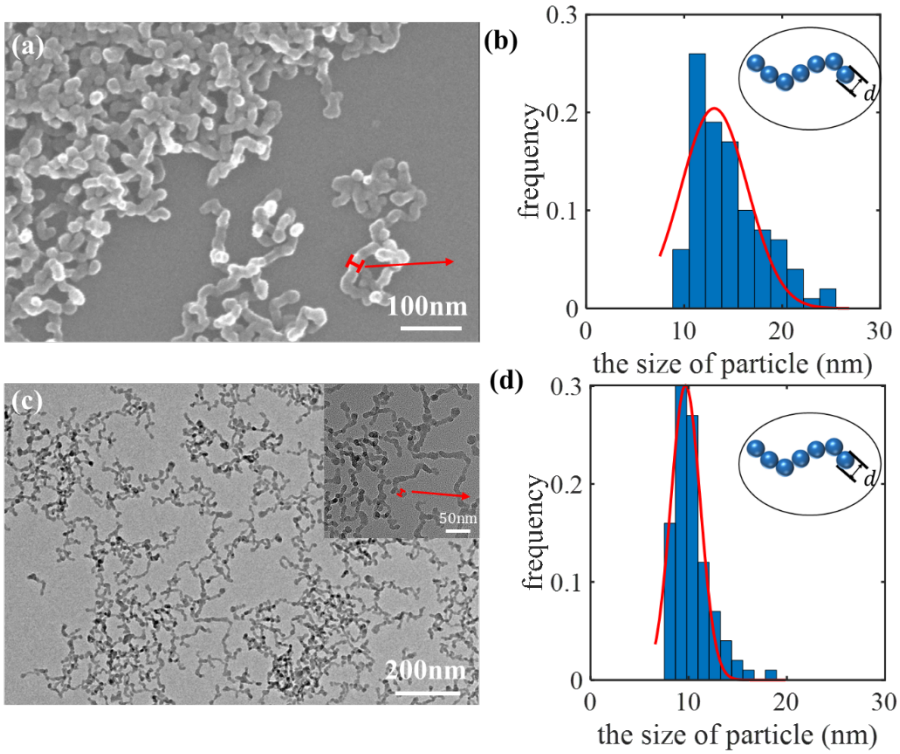

Figure S1. *Particle size distributions, SEM and TEM micrographs of chain-like particles. (a) SEM image of chain-like particles.* (b) Particle size distribution from the SEM micrograph.(c) TEM images of chain-like particles. (d) Particle size distribution from the TEM micrograph.

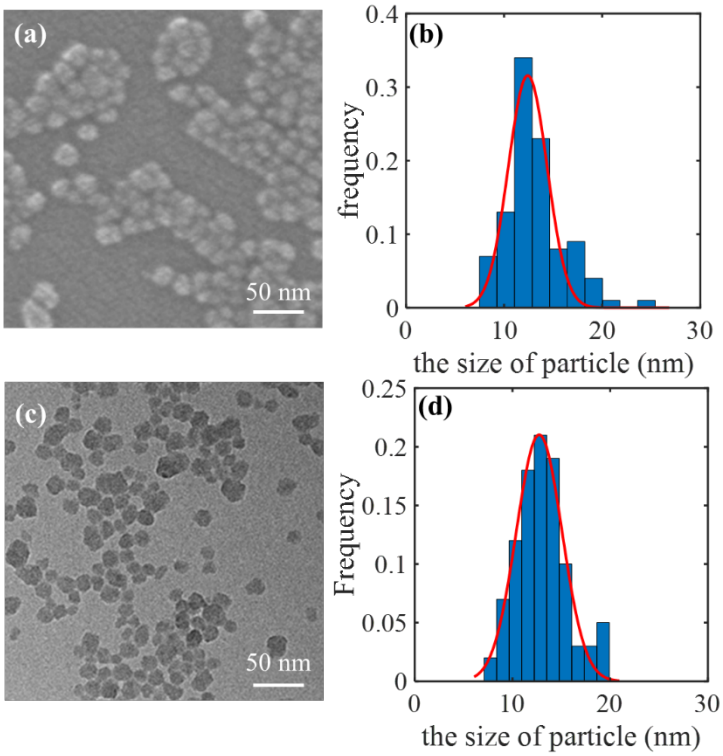

Figure S2. *Particle size distributions, SEM and TEM micrographs of sphere silica. (a) SEM image of sphere colloidal particles.* (b) Particle size distribution from the SEM micrograph.(c) TEM image of sphere colloidal particles. (d) Particle size distribution from the TEM micrograph.

Setup of drying experiments and characterization of crack patterns

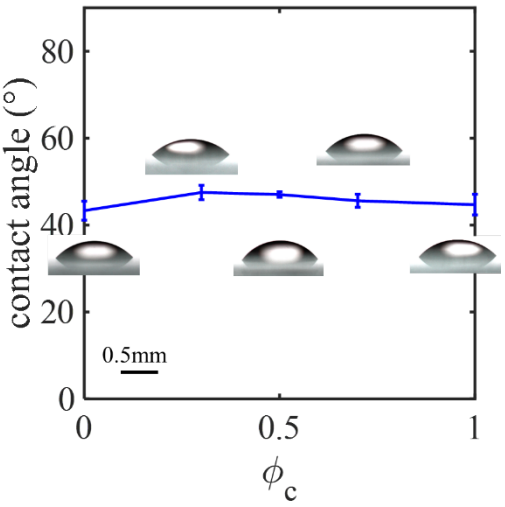

Figure S3. *Contact angles of colloidal suspension drop with different* ϕ_c (0, 0.3, 0.5, 0.7, and 1). The drops are dried on the glass cover slice as a drop.

The colloidal suspensions were dropped and then dried on a 12-well plate, as depicted in Figure S4. By imaging a 1 μL drop on the bottom of the well plate, we estimated the contact angles of the colloidal suspensions as a function of ϕ_c (see Figure S5). It is observed that the contact angles range between 80° and 90°, contributing to form uniform and thick films[1]. It indicuates that the colloidal suspensions in the well plates, although with various ϕ_c, exhibit the similar wetting property.

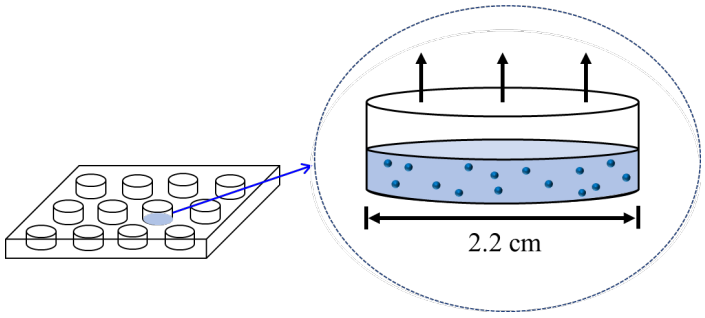

Figure S4. *The schematic drying experiment setup of a 12-well plate.*

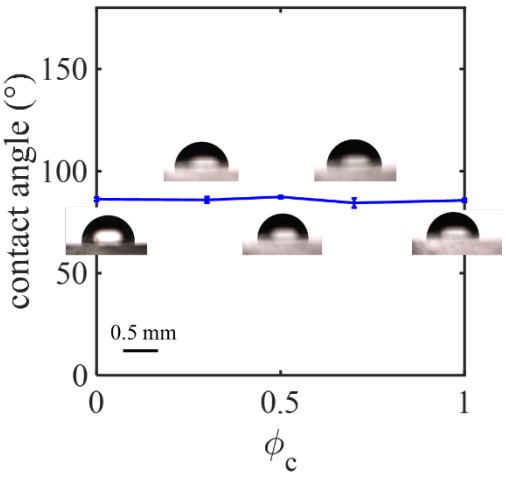

Figure S5. *Contact angles of colloidal suspension with* ϕ_c= 0, 0.3, 0.5, 0.7 *and 1, respectively.* They are dried on the 12-well plates.

Aftering drying in the well plates, we characterized the crack patterns of the colloidal deposits with different ϕ_c (see Figure S6). The result presents that increasing ϕ_c leads to a decrease of number of the cracks (see Figure S6a), although the initial suspension drops have the same volume (1500 μL) and concentration (16 wt. %). Meanwhile, the deposit thickness increases slightly for large values of ϕ_c, as shown in Figure S6(b). Moreover, we conducted another set of experiments where the deposit thickness is controlled by adjusting the volume of initial suspension drop (see Figure S6d). Figure S6(c) shows a similar tendency that the crack number decreases as ϕ_c increases. Therefore, the similar transitions of crack number over ϕ_c were obtained for the colloidal deposits dried in the 12-well plate and for those dried on the glass cover. Such a result suggests that the role of chain-like particles on suppressing cracks in colloidal deposits is not dependent on the drying methods.

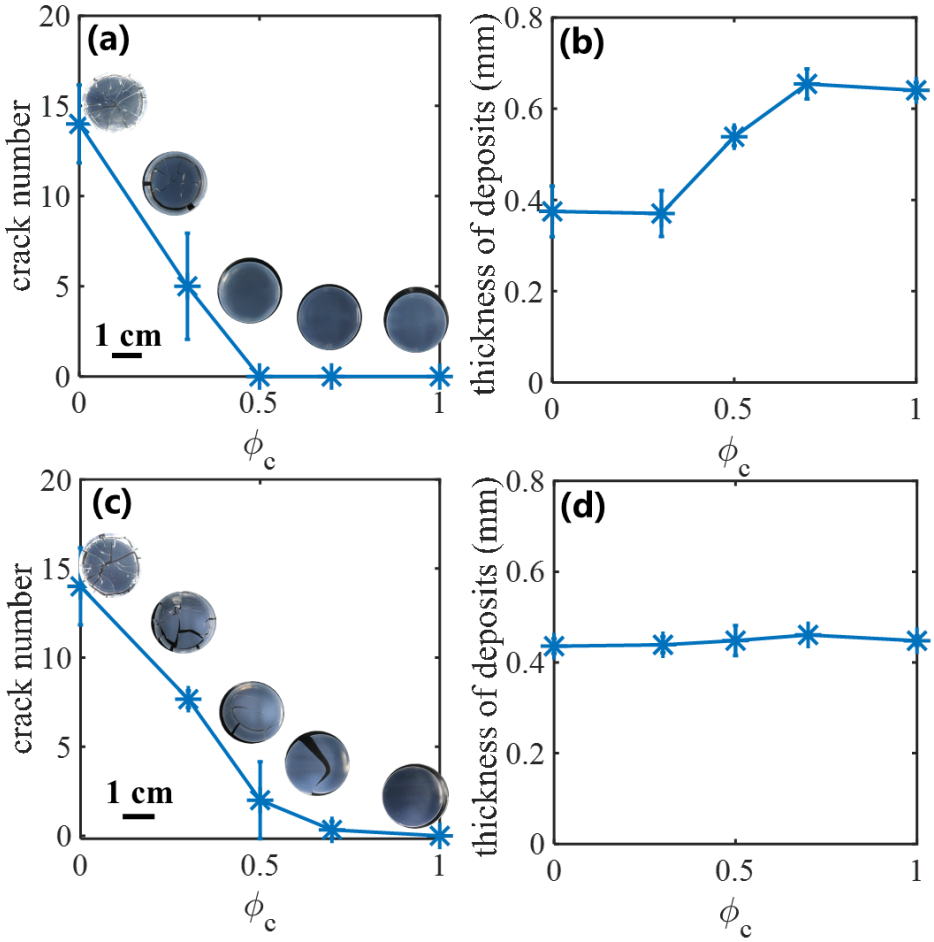

Figure S6. *The crack patterns, crack number, and the corresponding thickness of colloidal deposits.* (a) Crack patterns and numbers and (b) corresponding deposit thickness as a function of ϕ_c for the case that the inital suspension drops have the same volume and concentration. (c) Crack patterns and numbers and (d) corresponding deposit thickness as a function of ϕ_c for the case that the inital suspension drops have various volumes and concentrations.

Microstructure of colloidal deposits with chain-like particles.

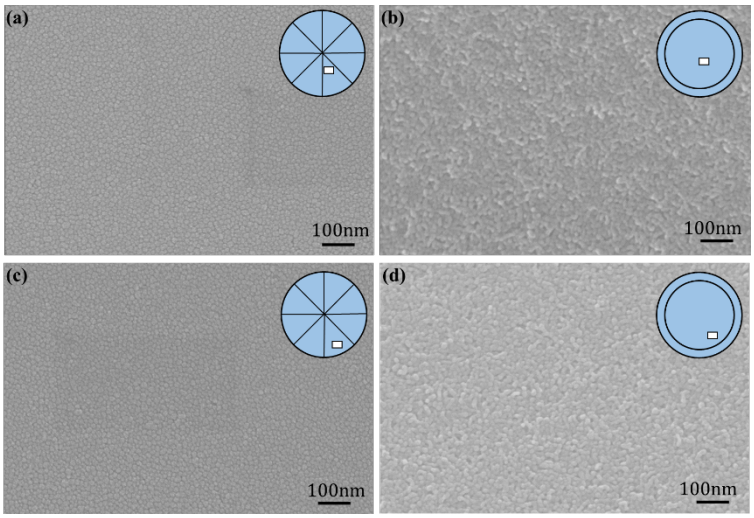

Figure S7. *Representative SEM micrographs taken near the center and edge of the colloidal deposits for different values of* ϕ_c. (a,b) shows the SEM micrographs taken near the center of the colloidal deposits for $\phi_c = 0$ and 1, respectively. (c,d) shows the SEM micrographs taken near the edge of the colloidal deposits for $\phi_c = 0$ and 1, respectively.

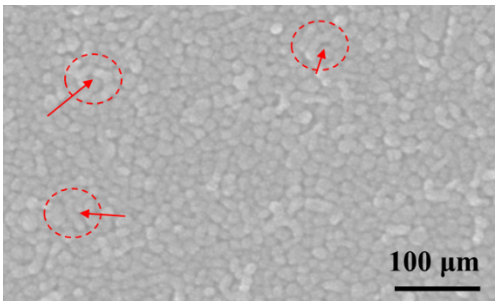

Figure S8. *Representative SEM micrographs of colloidal deposits with* $\phi_c = 0.5$ *after drying on the 12-well plates.*

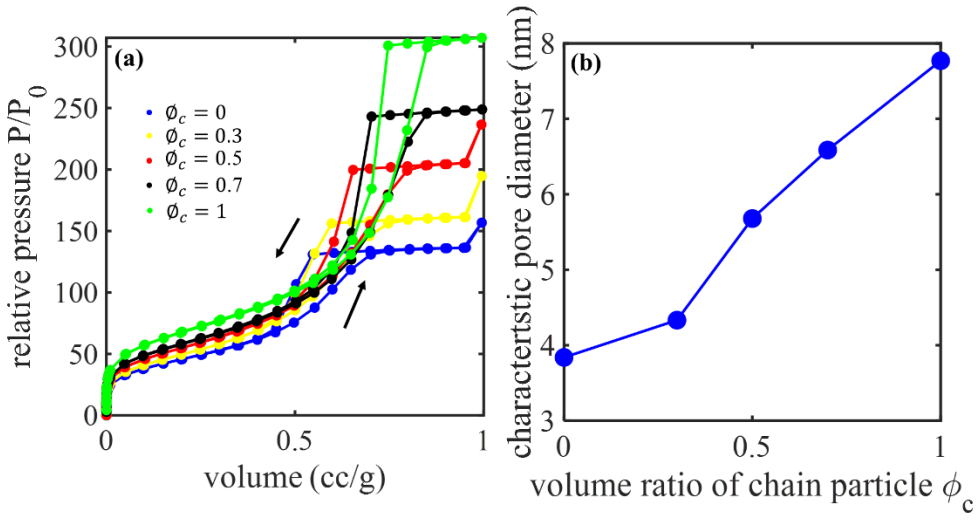

Figure S9. *Pore structure of the colloidal deposits obtained from nitrogen adsorption-desorption experiment.* (a) The nitrogen adsorption-desorption isotherms of colloidal deposits with ϕ_c= 0, 0.3, 0.5, 0.7, and 1. (b) Characteristic pore size, i.e., the peak value of pore size distributions, as a function of ϕ_c.

To calculate the stress distribution, the colloidal deposit can be assumed as an isotropic linear poroelastic axisymmetric cylindrical symmetry (r, θ, z). Inside the deposit, the liquid pressure P_L satisfies the Laplace equation:

$$\nabla^2 P_L(r) = 0 \tag{S1}$$

When the thickness of the colloidal deposits is smaller than the radius, the liquid pressure evolves mainly in the radial direction and is negligible across the thickness. Therefore, the liquid pressure P_L can be expressed by the 1D-diffusion equation:

$$\frac{\eta}{kE}\frac{\partial P_L(r)}{\partial t} = \nabla^2 P_L(r), \tag{S2}$$

where k is permeability, E the elastic modulus of colloidal deposits and η the viscosity of solvent. Based on the Eqs.(S1), (S2) as well as the boundary conditions stated in main text for Eq.(2) and Eq.(3), the liquid pressure is solved as follows:

$$P_L(r) = -\frac{J_s \eta r_e}{k}\ln\left(\frac{r}{r_e}\right) - P_{max}. \tag{S3}$$

The equilibrium equation relating the radial stress, hoop stress and axial stress can be given as follows:

$$\sigma_\theta = \sigma_r + r\frac{\partial \sigma_r}{\partial r}, \tag{S4}$$

$$\frac{\partial \sigma_\theta}{\partial r} = 0, \tag{S5}$$

$$\frac{\partial \sigma_z}{\partial z} = 0. \tag{S6}$$

Biot's constitutive relation[2] can give the relationship between the stain, stress, and liquid pressure:

$$\epsilon_r = \frac{1}{E}[\sigma_r - \nu(\sigma_\theta + \sigma_z)] + \frac{P_L}{3K}, \tag{S7}$$

$$\epsilon_\theta = \frac{1}{E}[\sigma_\theta - \nu(\sigma_r + \sigma_z)] + \frac{P_L}{3K}, \tag{S8}$$

$$\epsilon_z = \frac{1}{E}[\sigma_z - \nu(\sigma_r + \sigma_\theta)] + \frac{P_L}{3K}, \tag{S9}$$

Where E, ν, and K are Young's modulus, Poisson's ratio, and bulk modulus ($K=E/3(1-2\nu)$) of the colloidal deposits, respectively.

We noted that for the geometry in current work, there is no stress in the z-direction. Therefore,

$$\sigma_z = 0. \tag{S10}$$

The boundary condition for the radial stress is:

$$\sigma_r|_{r=r_e} \approx 0. \tag{S11}$$

The colloidal deposits are strongly adhered on the stiff substrate. Therefore, the axial stain is greater than the sum of the lateral strains, resulting in:

$$\epsilon_z \gg \epsilon_r + \epsilon_\theta. \tag{S12}$$

According to Eq.(S10), Eq.(S9) can be writtern as follows:

$$\epsilon_z = -\frac{\nu}{E}(\sigma_r + \sigma_\theta) + \frac{P_L}{3K}. \tag{S13}$$

According to Eqs.(S7-S10) and Eq.(S12), the sum of strains can be expressed as:

$$\epsilon_z = \frac{1}{3K}(\sigma_r + \sigma_\theta) + \frac{P_L}{K}. \tag{S14}$$

By combining Eq.(S13) and Eq.(S14), we obtain that:

$$\sigma_r + \sigma_\theta = AP_L(r), \tag{S15}$$

where $A = -\frac{2}{3K(\frac{1}{3K}+\frac{v}{E})}$. Then, by substituting Eqs.(S2) and (S4) into (S15), we obtain:

$$\frac{d}{dr}(r^2\sigma_r) = Brln\left(\frac{r}{r_e}\right) - ArP_{max}, \tag{S16}$$

where, $B = -\frac{Ar_eJ_s\eta}{k}$. Now, by integrating both side of the Eq.(S16) and substituting Eq.(S11) and liquid pressure Eq.(S2), we obtain:

$$\sigma_r = B\left(\frac{1}{2}ln\frac{r}{r_e} - \frac{1}{4} + \frac{r_e^2}{4r^2}\right) - \frac{AP_{max}}{2}\left(1 - \frac{r_e^2}{r^2}\right). \tag{S17}$$

The hoop stress is written as:

$$\sigma_\theta = B\left(\frac{1}{2}ln\frac{r}{r_e} + \frac{1}{4} - \frac{r_e^2}{4r^2}\right) - \frac{AP_{max}}{2}\left(1 + \frac{r_e^2}{r^2}\right). \tag{S18}$$

The stresses of colloidal deposits with various ϕ_c can be determined by substituting the distinct packing fraction ψ_d measured in experiment, r_e observed from the microscopy images, the consistent evaporate rate $J_s \simeq 4.7\times10^{-7}$m/s, the consistent radius of sphere particle $a \sim 6.5$ nm, $\eta \sim 0.001$ Pa·s, and Poisson's ratio[3] $v \sim 0.2$.

Critical cracking thickness and mechanical properties of colloidal deposits with chain-like particles

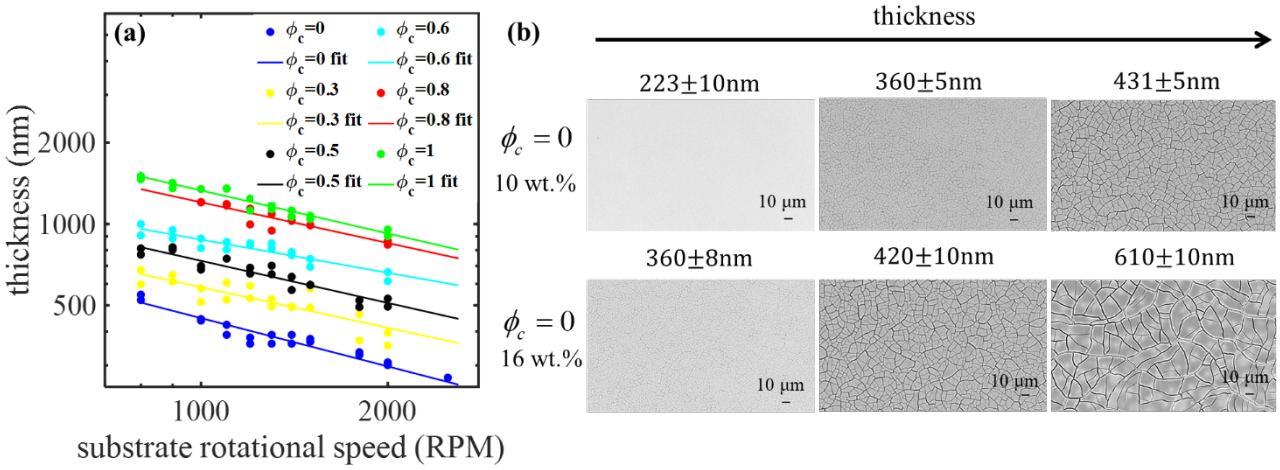

Figure S10. *Thickness of colloidal deposits with different ϕ_c obtain by varying the substrate rotational speed and initial concentration.* (a) Thickness as a function of rotational rate for colloidal deposits with different ϕ_c. The thickness of colloidal deposits decreases exponentially with the rising rotational speed. Percentages given as labels within the plot are the intial suspension concentrations of colloidal particle in % by wt. (b) Optical microscope images of colloidal deposits with various thickness at the initial concentration 10 wt. % and 16 wt. % ($\phi_c = 0$). For the colloidal deposits with $\phi_c = 0$, the thinner colloidal deposits is obtained by decreasing the initial concentration of colloidal particles.

The critical cracking thickness (CCT) can be predicted by the critical stress model. The multiplying factor in Eq. (8) of the main text is increased by a factor of 4 (compared to 2 in previous work) in obtaining Eq. (9) in our work, facilitating a comparison with the experimental data[4].

Within the theoretical model, the predicted CCT can be affected by the coordination number, pore diameter, and packed structure of chain-like particles. In Figure 4(b), the predicted CCT is calculated using the same coordination number of 5. However, the real

coordination number may vary with ϕ_c in colloidal deposits. In our experiment, ψ_d in colloidal deposits ranges from 0.58 to 0.42. Correspondingly, the coordination number typically varies between 4 and 6 [5]. Such a fluctuation in coordination numbers does not significantly modify the overall trend, but only affects the specific numerical values of CCT. In addition, a uniform capillary radius, corresponding to the radius of spherical particles, is utilized to calculate the maximum capillary pressure in colloidal deposits with different ϕ_c. If we modify the maximum capillary pressure by taking the characteristic pore diameter (in Figure S9b) as the capillary radius, the range of the predicted CCT will expand. This expansion is attributed to the influence of the capillary radius on the corresponding capillary pressure. Furthermore, the cross and intertwine packing of chain-like particles in colloidal deposits may inhibit the creation of new surfaces during the crack formation, potentially resulting in the lower predicted CCT than the measured CCT. Hence, as compared with the experimentally measured CCT, the range of the predicted CCT may become narrower.

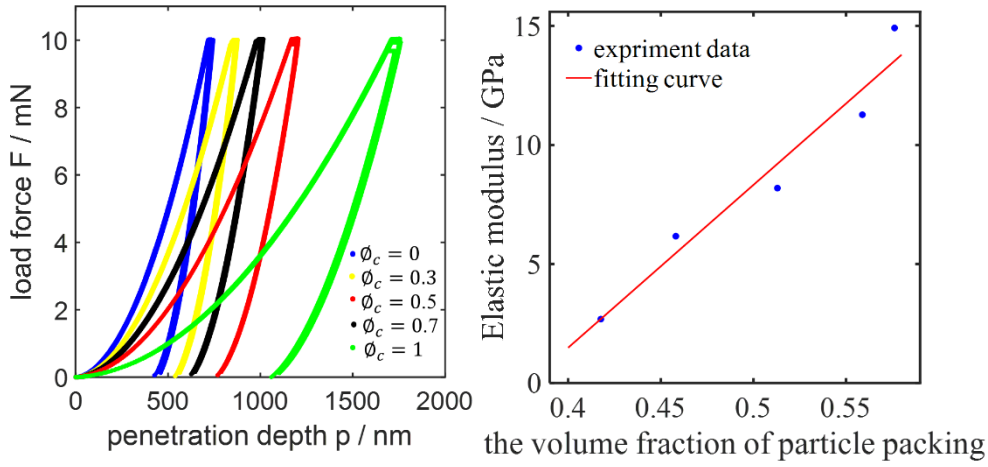

Figure S11. *Mechanical properties of colloidal deposits with ϕ_c. (a) The curve of load and unload force versus the penetration.* (b) The experiment measured elastic modulus versus the packing fraction of particles in colloidal deposit with different ϕ_c and the corresponding fitted curve.

References

[1] H. Zargartalebi, S.H. Hejazi, and A. Sanati-Nezhad, "Self-assembly of highly ordered micro- and nanoparticle deposits," Nat Commun **13**(1), 1–11 (2022).

[2] M.A. Biot, "General Theory of Three-Dimensional Consolidation," J. Appl. Phys. **12**(2), 155–164 (1941).

[3] M. Léang, F. Giorgiutti-Dauphiné, L.-T. Lee, and L. Pauchard, "Crack opening: from colloidal systems to paintings," Soft Matter **13**(34), 5802–5808 (2017).

[4] K.B. Singh, and M.S. Tirumkudulu, "Cracking in Drying Colloidal Films," Phys. Rev. Lett. **98**(21), 218302 (2007).

[5] K. Yasuda, F. Takase, and Y. Matsuo, "Stochastic analysis on coordination number distribution of particles during powder compaction," Adv. Powder Technol. **24**(5), 871–878 (2013).